Article ID: 1000-7032(2022)09-1428-08

Crystal-field Splitting in Regular Polyhedron

SONG Zhen*, LIU Quan-lin*

(*Beijing Key Laboratory for New Energy Materials and Technologies, School of Materials Science and Engineering, University of Science and Technology Beijing, Beijing* 100083, *China*)

* *Corresponding Authors, E-mail: zsong@ustb. edu. cn; qlliu@ustb. edu. cn*

Abstract: Crystal-field theory plays a fundamental role in understanding the energy levels of rare-earth and transition-metal elements in inorganic hosts. It has been fully developed for the octahedral field, both in analytical energy level expression and pictorial understanding. Nevertheless, the crystal field theory for other regular cubic polyhedra, including tetrahedron, cube and cuboctahedron, needs further investigation to show the similarities and differences with the octahedral field. In this work, the detailed crystal-field analysis of one d electron in those regular polyhedra is presented using the perturbation method. The exact crystal-field potentials are derived based on geometrical models with equivalent center-ligand bond length. The secular matrices are constructed and diagonalized to give the split energy levels. The crystal-field splittings for regular tetrahedron, octahedron, cube and cuboctahedron are calculated to be $40Dq/9$, $90Dq/9$, $80Dq/9$ and $45Dq/9$. In the end, the relative orientations between e_g/t_{2g} orbitals and the ligands are visualized to present a vivid understanding of the magnitude reverse.

Key words: crystal field; energy level; splitting; polyhedron

CLC number: O482. 31　　**Document code**: A　　**DOI**: 10. 37188/CJL. 20220190

正多面体中的晶体场劈裂

宋　振*, 刘泉林*

(北京科技大学 材料科学与工程学院, 北京市新能源材料与技术重点实验室, 北京　100083)

摘要: 晶体场理论是理解稀土/过渡金属离子在无机固体中能级结构的关键。对八面体场,能级表达式及图像解释发展得较为完善,但正四面体、立方体和立方八面体中的能级劈裂情况则需要进一步明确。本文根据微扰理论详细推导了单d电子在上述规则多面体中的晶体场劈裂。基于等键长的几何模型,给出了晶体场势的准确形式。随后构建了久期方程并通过对角化得到了劈裂后的能级。正四面体、八面体、立方体和立方八面体的晶体场劈裂大小分别为$40Dq/9$、$90Dq/9$、$80Dq/9$和$45Dq/9$。最后,d电子轨道与配位离子的相对取向关系有助于形象地理解e_g/t_{2g}能级在不同正多面体中的反转现象。

关　键　词: 晶体场; 能级; 劈裂; 多面体

1　Introduction

Research on luminescent materials has greatly promoted the development of optoelectronic devices in recent years[1-3]. Rare-earth or transition metal elements doped phosphors contribute a major part in solid-state lighting. Spectroscopic modulation has been widely investigated for those phosphors to meet the application requirements, such as adding red-

收稿日期: 2022-05-09; **修订日期**: 2022-05-21

基金项目: 国家自然科学基金(51832005,51972020); 中央高校基本科研业务费专项资金(FRF-IDRY-20-028)资助项目

Supported by National Natural Science Foundation of China(51832005,51972020); Fundamental Research Funds for The Central Universities(FRF-IDRY-20-028)

light component to improve the lighting quality[4-5]. Generally, the luminescence tuning is implemented by host structure variation through composition substitution[6]. The guideline is derived from crystal-field theory, which describes the Stark effect of outer-shell valence electrons embedded in the electrostatic potential field originating from the neighboring anionic ligands. The crystal-field effect of one d electron embedded in 6-coordinated octahedron with point symmetry O_h has been thoroughly investigated, from which a general rule about the bond length and the energy level splitting is derived to relate the spectroscopy with structure variation[7]. It reflects the reciprocal relationship between 5th-power of bond length and the magnitude of the crystal-field splitting[8-9]. Although there exist several exceptions, this rule has been widely applied in understanding the structure-property relationship in luminescent materials.

The simple 5th-power rule is derived for the 6-coordinated octahedron, which bears point symmetry O_h. There also exist some other regular polyhedra belonging to the same symmetry, *i. e.*, 4-coordinated tetrahedron[10], 8-coordinated cube[11] and 12-coordinated cuboctahedron[12]. Meanwhile, those polyhedra are suitable for luminescent dopant ions to reside in. For example, transition-metal ions prefer the smaller tetrahedron and octahedron, whereas rare-earth elements are usually found in larger cube or cuboctahedron[13-14]. The crystal-field effects in all those regular cubic polyhedra share the same 5th-power reciprocal rule but differ in the splitting magnitude[15]. In addition, the split energy levels are sorted reversely among those polyhedra. For example, the splitting of one d electron in the 6-coordinated octahedron has two high-lying e_g orbitals ($d_{x^2-y^2}$, d_{z^2}) and three low-lying t_{2g} orbitals (d_{xy}, d_{yz}, d_{xz}) due to crystal-field splitting, which could be described pictorially from the arrangements of orbital lobes towards ligand anions[16]. Meanwhile, the sorting of e_g and t_{2g} orbitals are reversed in the 8-coordinated cube potential, together with a shrinkage in the energy-level difference. For tetrahedron and cuboctahedron, the investigations on crystal-field splitting magnitude and relative order of energy levels are less reported, and until now the pictorial description of orbital arrangements regarding ligands is still unclear as far as we know.

Analysis on luminescence tuning often relies on the understanding of crystal-field splitting in those regular polyhedra. For example, the photoluminescent excitation spectra of Ce^{3+} in 8-coordination environment reveal two peaks near the low-energy side, which correspond to the two low-lying e_g orbitals[17-18]. In multi-site structure such as garnet[19-20], spinel and pyrochlore[21-22], researchers need to compare the crystal-field strength of different coordination polyhedra to identify the cationic site-occupancy. Therefore, in this work we provide a detailed analysis of crystal-field effects of d^1 electron in regular cubic polyhedra using perturbation theory. The magnitudes of crystal-field splitting are given, together with the sorting order of the energy levels, and the orbitals are visualized together with the ligands. We hope this work could clarify the misconceptions and serve as a reference for chemists, physicists, spectroscopists and material scientists in the field of luminescent materials.

2 Methods

2.1 Geometrical Models of Regular Cubic Polyhedron

We set up the models of 4 types of regular cubic polyhedra, *i. e.*, tetrahedron, octahedron, cube, and cuboctahedron. Their centers are set as the origin of the Cartesian coordinate system, which is reserved to accommodate the dopant luminescent ion. The ligand coordinates of all the polyhedra are $\frac{1}{\sqrt{3}}\{(a, -a, -a), (-a, a, -a), (a, a, a), (-a, -a, a)\}$ for tetrahedron, $\{(a, 0, 0), (-a, 0, 0), (0, a, 0), (0, -a, 0), (0, 0, a), (0, 0, -a)\}$ for octahedron, $\frac{1}{\sqrt{3}}\{(a, a, a), (a, -a, a), (-a, a, a), (-a, -a, a), (a, a, -a), (a, -a, -a), (-a, a, -a), (-a, -a, -a)\}$ for cube, $\frac{1}{\sqrt{2}}\{(a, 0, a), (0, a, a), (a, a, 0), (0, -a, a), (a, -a, 0), (-a, 0, a), (-a, a, 0), (-a, -a, 0), (a, 0, -a), (0, a, -a), (0, -a, -a), (-a, 0, -a)\}$ for cuboctahedron. Those ligand coordinates are set to

ensure that all the polyhedra share the same center-vertex length a. The aim is to investigate the effect of coordination number on the splitting magnitude at the same bond length.

2.2 Expressing Crystal-field Potentials

Although all the regular cubic polyhedra belong to point symmetry O_h, their corresponding crystal-field potentials differ in algebraic expression. Let the ligand has charge Ze, then the electrostatic potential between the electron and the ligand is $V = \frac{Ze^2}{a}$. It could be further rewritten with the help of Legendre polynomials $P_l(\cos\theta')$ as

$$V = \frac{Ze^2}{a}\sum_{l=0}\left(\frac{R}{a}\right)P_l(\cos\theta'), \tag{1}$$

in which l is no larger than 4 for d electron and $R = \sqrt{x^2+y^2+z^2}$ is the distance between the origin and electron with coordinates (x, y, z). Every ligand has a potential calculated by its own coordinates, and the sum of all the ligand potentials is the crystal-field potential. The final expression could be simplified by selecting

$$D = \frac{35Ze^2}{4a^5}, \tag{2}$$

this assignation was first introduced for the crystal-field splitting in octahedron[7], and also serves as the origin of 5th-power relationship. In this work, the definition of D is preserved for all the regular polyhedra. The expressions of crystal-field potential are listed in Tab. 1

Tab. 1 Crystal-field potential expressed by electron coordinates (x, y, z)

Polyhedron type	Crystal-field potential
Tetrahedron	$\frac{4e^2Z}{a} + D\left[-\frac{2R^4}{5} + \frac{2}{63}\left(7x^4+7y^4+7z^4+42x^2y^2+42y^2z^2+42x^2z^2+24\sqrt{3}\,axyz\right)\right]$
Octahedron	$\frac{6e^2Z}{a} + D\left(-\frac{3R^4}{5} + x^4+y^4+z^4\right)$
Cube	$\frac{8e^2Z}{a} + D\left[-\frac{4R^4}{5} + \frac{4}{9}\left(x^4+y^4+z^4+6x^2y^2+6y^2z^2+6x^2z^2\right)\right]$
Cuboctahedron	$\frac{12e^2Z}{a} + D\left[-\frac{6R^4}{5} + x^4+y^4+z^4+3x^2y^2+3y^2z^2+3x^2z^2\right]$

2.3 Construction of Perturbation Secular Matrix

The crystal-field splitting is caused by the Stark effect of the ligands. The changes in energy levels could be evaluated by the first-order perturbation energy $\langle\Psi_{nlm}|V|\Psi_{nlm}\rangle$ by means of the d electron wavefunction $\Psi_{nlm} = R_{nl}(r)Y_m^l(\theta,\phi)$, in which R_{nl} is the radial part, Y_m^l the angular part represented by the spherical harmonics. The wavefunctions of d electron with l =2 and m_l=2, 1, 0, −1, −2 are 5-fold degenerated before applying the crystal-field potential perturbation, therefore the perturbation matrix with a total of 25 elements needs pre-evaluation before diagonalization. The matrix element could be expanded as

$$\begin{aligned}\langle\Psi_{nlm}|V|\Psi_{nlm}\rangle &= \int_0^\infty\int_0^\pi\int_0^{2\pi} R_{nl}(R)\Theta_{lm}(\theta)\Phi_m(\phi)VR_{nl'}(R)\Theta_{l'm'}(\theta)\Phi_{m'}(\phi)R^2\sin\theta\mathrm{d}R\mathrm{d}\theta\mathrm{d}\phi \\ &= \langle R_{nl}|V(R)|R_{nl'}\rangle\langle lm|V(\theta,\phi)|lm'\rangle,\end{aligned} \tag{3}$$

in which the angular part could be integrated but the radial part needs parametric substitution of

$$q = \frac{2}{105}\int_0^\infty R_{nl}^2(R)R^4R^2\mathrm{d}R = \frac{2}{105}\langle R^4\rangle, \tag{4}$$

the residual R^2 in the integral is used for normalization of R_{nl}. Now we have the full expression of Dq, which is

$$Dq = \frac{Ze^2\langle R^4\rangle}{6a^5}, \tag{5}$$

it has the energy scale, usually in wavenumber. Finally, the secular matrix could be expressed only by the product of two parameters Dq, as listed in Tab. 2. Diagonalization of those matrices provides eigenvalues and eigenfunctions in Tab. 3. It should be noted that all the regular polyhedra share the same Dq, because they are modelled with the equivalent center-vertex length a. As a result, those crystal-field

Tab. 2 Perturbation seculiar matrix constructed by eigenfunctions of d electron

Tetrahedron	$m_l = 2$	1	0	−1	−2
$m_l = 2$	$-\frac{4Dq}{9}$				$-\frac{20Dq}{9}$
1		$\frac{16Dq}{9}$			
0			$-\frac{8Dq}{3}$		
−1				$\frac{16Dq}{9}$	
−2	$-\frac{20Dq}{9}$				$-\frac{4Dq}{9}$
Octahedron	$m_l = 2$	1	0	−1	−2
$m_l = 2$	Dq				$5Dq$
1		$-4Dq$			
0			$6Dq$		
−1				$-4Dq$	
−2	$5Dq$				Dq
Cube	$m_l = 2$	1	0	−1	−2
$m_l = 2$	$-\frac{8Dq}{9}$				$-\frac{40Dq}{9}$
1		$\frac{32Dq}{9}$			
0			$-\frac{16Dq}{3}$		
−1				$\frac{32Dq}{9}$	
−2	$-\frac{40Dq}{9}$				$-\frac{8Dq}{9}$
Cuboctahedron	$m_l = 2$	1	0	−1	−2
$m_l = 2$	$-\frac{Dq}{2}$				$-\frac{5Dq}{2}$
1		$2Dq$			
0			$-3Dq$		
−1				$2Dq$	
−2	$-\frac{5Dq}{2}$				$-\frac{Dq}{2}$

Tab. 3 Diagonalization results of the seculiar matrix and the total crystal-field splitting

Orbitals		Tetrahedron	Octahedron	Cube	Cuboctahedron
e_g	$d_{x^2-y^2}$	$-\frac{8Dq}{3}$	$6Dq$	$-\frac{16Dq}{3}$	$-3Dq$
	d_{z^2}	$-\frac{8Dq}{3}$	$6Dq$	$-\frac{16Dq}{3}$	$-3Dq$
t_{2g}	d_{xy}	$\frac{16Dq}{9}$	$-4Dq$	$\frac{32Dq}{9}$	$2Dq$
	d_{xz}	$\frac{16Dq}{9}$	$-4Dq$	$\frac{32Dq}{9}$	$2Dq$
	d_{yz}	$\frac{16Dq}{9}$	$-4Dq$	$\frac{32Dq}{9}$	$2Dq$
Total splitting		$\frac{40Dq}{9}$	$\frac{90Dq}{9}$	$\frac{80Dq}{9}$	$\frac{45Dq}{9}$

splittings are comparable.

3 Results and Discussion

The results in Tab. 3 are visualized in Fig. 1, denoting the perturbed energy levels of e_g and t_{2g} orbitals with regard to the unperturbed one with 5-fold degeneration. They are presented in the sequence of largr polyhedral coordination number. Since the point symmetries of all the polyhedra belong to the point symmetry O_h, it is expected from group theory that the 5-degenerated levels of d^1 electron will be split into e_g and t_{2g} orbitals with 2 and 3 degeneration, respectively, *i. e.*, $D^{(2)} = e_g \oplus t_{2g}$. This scheme is confirmed in Fig. 1. Solving the perturbation matrix further gives the quantities of both crystal-field levels, and their values differ in magnitude. In general, the total crystal-field splitting is decreasing as the polyhedron has more coordination number, except tetrahedron which has the smallest one. Octahedron has the largest $10Dq$ with the e_g orbital positioned higher than the t_{2g} one, whereas all the other polyhedra have the opposite energy level sequence. For tetrahedron, the crystal-field splitting is 4/9 of that in octahedron, which is consistence with previous reports[23-24]. Nevertheless, the magnitude ratio of the split energy levels keeps 2∶3. There also exist duple relationships among the crystal-field splittings of tetrahedron/cube$\left(\frac{40Dq}{9} : \frac{80Dq}{9} = 1 : 2\right)$, and cuboctahedron/octahedron$\left(\frac{45Dq}{9} : \frac{90Dq}{9} = 1 : 2\right)$. It is a coincidence that the coordination number is doubled and half reduced in both cases.

The eigenfunctions could also be obtained by matrix diagonalization, and they are linearly combined into the d-electron orbitals and visualized in the frame of polyhedral ligands as shown in Fig. 2 – Fig. 5. As the well-known energy level sequence in octahedron suggests (Fig. 3), those orbitals with lobes directed away from the ligand are positioned lower in the energy scale. For tetrahedron in Fig. 2, the lobes of t_{2g} orbitals are positioned near the ligands, whereas those of e_g orbitals are directed towards the gap between two adjacent ligands.

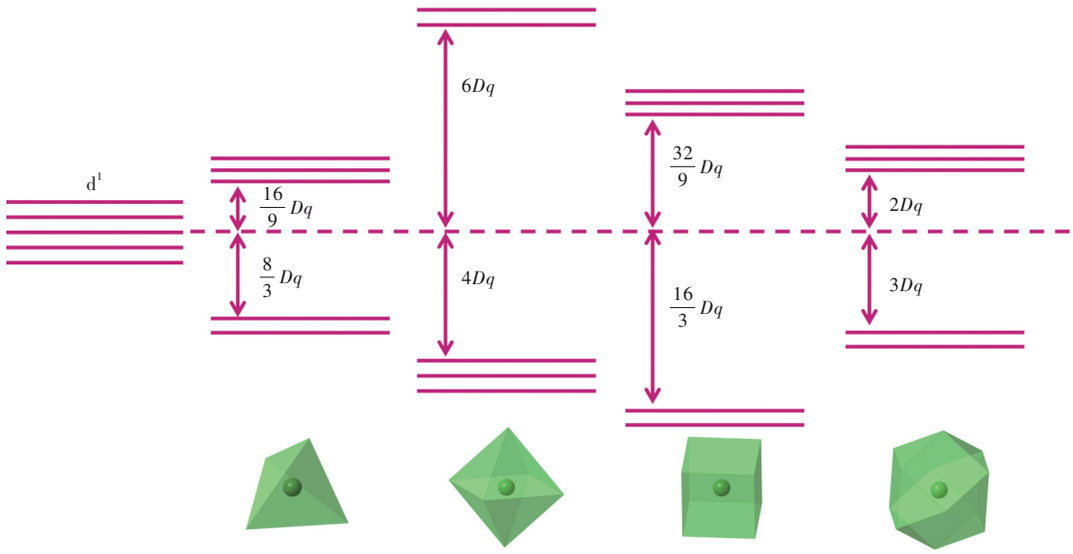

Fig. 1 Crystal-field splitting of d^1 electron in various polyhedral potentials. The dashed line represents the 5-fold unsplit energy levels.

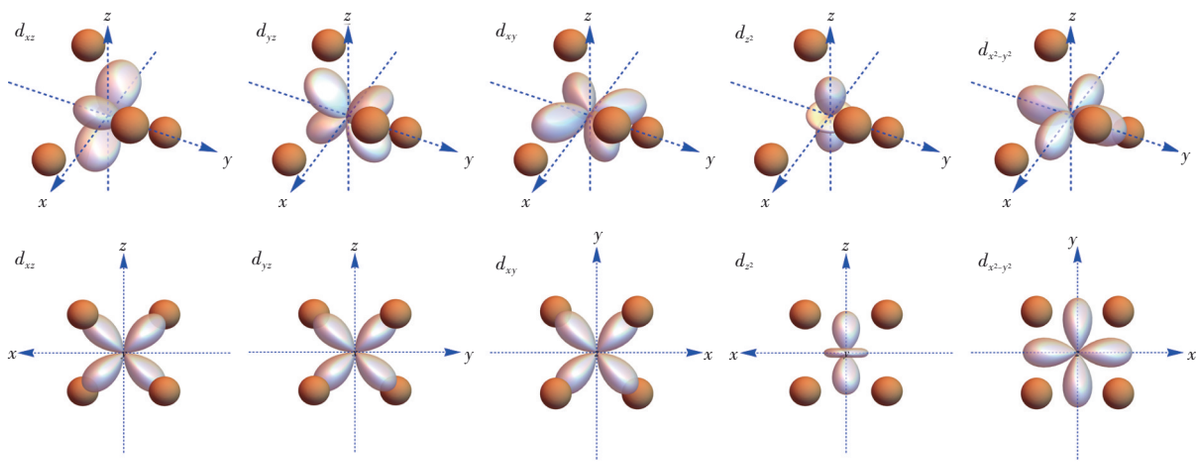

Fig. 2 Visualization of d-electron orbitals in the frame of tetrahedral ligands. Up: stereo views. Down: views along [010], [100], [001], [010] and [001] directions, respectively.

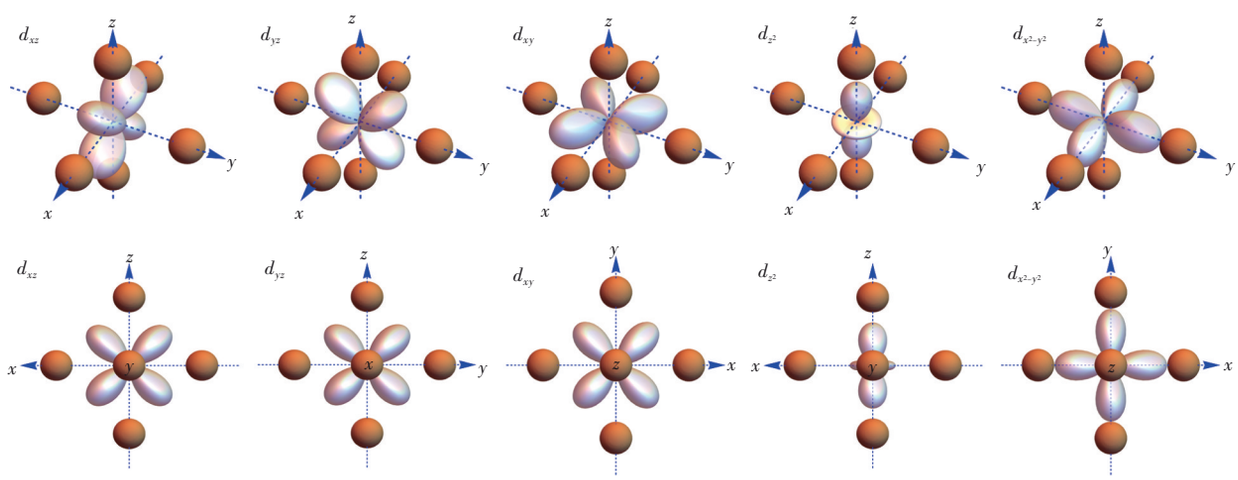

Fig. 3 Visualization of d-electron orbitals in the frame of octahedral ligands. Up: stereo views. Down: views along [010], [100], [001], [010] and [001] directions, respectively.

Therefore, tetrahedron has low-lying e_g orbitals. For cube in Fig. 4, the t_{2g} orbitals are also pointed towards the gap, but the e_g orbitals have lobes directed into the virtual void surrounded by four neighboring ligands, which induces less electrostatic interaction with the ligand anions. Meanwhile, this kind of virtual void also explains the low-lying e_g orbitals in cuboctahedron (Fig. 5), of which the high-lying t_{2g} orbitals have lobes directed towards the ligand anion.

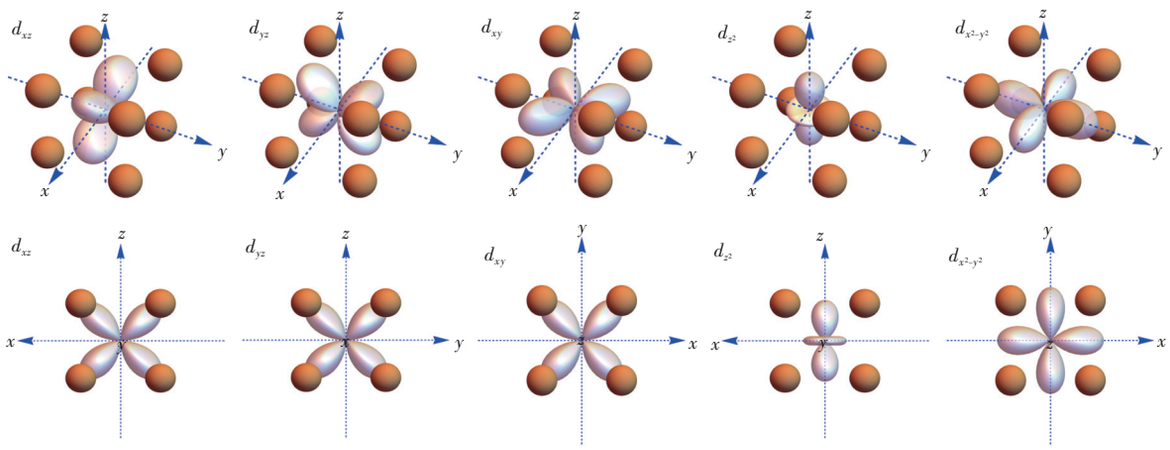

Fig. 4　Visualization of d-electron orbitals in the frame of cube ligands. Up: stereo views. Down: views along [010], [100], [001], [010] and [001] directions, respectively.

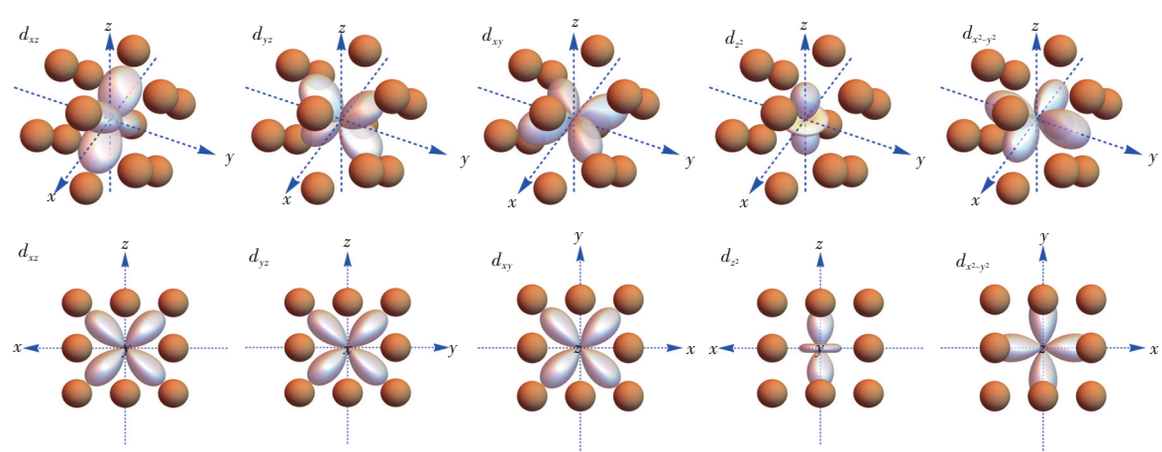

Fig. 5　Visualization of d-electron orbitals in the frame of cuboctahedral ligands. Up: stereo views. Down: views along [010], [100], [001], [010] and [001] directions, respectively.

4　Conclusion

In this work, the crystal-field effects in regular cubic polyhedra are analyzed in detail. The geometrical models are set up with equi-distant ligand for every polyhedron. Through perturbation theory, the total crystal-field splittings are expressed analytically as $\frac{40Dq}{9}$, $10Dq$, $\frac{80Dq}{9}$ and $\frac{45Dq}{9}$ for tetrahedron, octahedron, cube and cuboctahedron, respectively. The magnitude shows a descending trend with coordination number except tetrahedron. Meanwhile, there exist duple relationships between those splittings. Only octahedron has high-lying e_g and low-lying t_{2g} orbitals, whereas the other polyhedra have the opposite sorting sequence. For pictorial understanding, the d electron orbitals are visualized together with the polyhedral ligands. It is found that those orbitals with lobes directed towards 4-ligand void or 2-ligand gap have lower energy by avoiding electrostatic repulsion. This work provides a deeper understanding of the crystal-field theory of regular cubic polyhedra.

Response Letter is available for this paper at: http://cjl.lightpublishing.cn/thesisDetails#10.37188/CJL.20220190.

References:

[1] QIAO J W, ZHAO J, LIU Q L, *et al*. Recent advances in solid-state LED phosphors with thermally stable luminescence [J]. *J. Rare Earths*, 2019, 37(6): 565-572.

[2] 郑鹏, 丁国真, 解荣军. Ce^{3+}和 Eu^{2+}掺杂荧光材料的光猝灭机理研究进展[J]. 发光学报, 2021, 42(10): 1447-1457.
ZHENG P, DING G Z, XIE R J. Research progress on optical quenching of Ce^{3+}- and Eu^{2+}-doped luminescent materials [J]. *Chin. J. Lumin.*, 2021, 42(10): 1447-1457. (in Chinese)

[3] 张亮亮, 张家骅, 郝振东, 等. Cr^{3+}掺杂的宽带近红外荧光粉及其研究进展[J]. 发光学报, 2019, 40(12): 1449-1459.
ZHANG L L, ZHANG J H, HAO Z D, *et al*. Recent progress on Cr^{3+} doped broad band NIR phosphors [J]. *Chin. J. Lumin.*, 2019, 40(12): 1449-1459. (in Chinese)

[4] ZHANG N M, TSAI Y T, FANG M H, *et al*. Aluminate red phosphor in light-emitting diodes: theoretical calculations, charge varieties, and high-pressure luminescence analysis [J]. *ACS Appl. Mater. Interfaces*, 2017, 9(28): 23995-24004.

[5] QIAO J W, NING L X, MOLOKEEV M S, *et al*. Site-selective occupancy of Eu^{2+} toward blue-light-excited red emission in a $Rb_3YSi_2O_7$:Eu phosphor [J]. *Angew. Chem.*, 2019, 131(33): 11645-11650.

[6] LIN L T, NING L X, ZHOU R F, *et al*. Site occupation of Eu^{2+} in $Ba_{2-x}Sr_xSiO_4$(x=0-1.9) and origin of improved luminescence thermal stability in the intermediate composition [J]. *Inorg. Chem.*, 2018, 57(12): 7090-7096.

[7] DUNN T M, MCCLURE D S, PEARSON R G. *Some Aspects of Crystal Field Theory* [M]. New York: Harper & Row, 1965.

[8] CHEN M Y, XIA Z G, MOLOKEEV M S, *et al*. Tuning of photoluminescence and local structures of substituted cations in $xSr_2Ca(PO_4)_2$-$(1-x)Ca_{10}Li(PO_4)_7$:Eu^{2+} phosphors [J]. *Chem. Mater.*, 2017, 29(3): 1430-1438.

[9] WANG X J, FUNAHASHI S, TAKEDA T, *et al*. Structure and luminescence of a novel orange-yellow-emitting $Ca_{1.62}Eu_{0.38}Si_5O_3N_6$ phosphor for warm white LEDs, discovered by a single-particle-diagnosis approach [J]. *J. Mater. Chem.* C, 2016, 4(42): 9968-9975.

[10] 林贵, 罗琦, 陈茜, 等. $ZnAl_2O_4/CaAl_{12}O_{19}$:$Mn^{4+}$荧光粉制备与发光性能[J]. 发光学报, 2022, 43(4): 536-544.
LIN G, LUO Q, CHEN Q, *et al*. Preparation and luminescent properties of $ZnAl_2O_4/CaAl_{12}O_{19}$: Mn^{4+} phosphors [J]. *Chin. J. Lumin.*, 2022, 43(4): 536-544. (in Chinese)

[11] WANG X C, ZHAO Z Y, WU Q S, *et al*. Synthesis, structure and photoluminescence properties of $Ca_2LuHf_2(AlO_4)_3$: Ce^{3+}, a novel garnet-based cyan light-emitting phosphor [J]. *J. Mater. Chem.* C, 2016, 4(48): 11396-11403.

[12] SONG Z, LIU Q L. Effect of polyhedron deformation on the 5d energy level of Ce^{3+} in lanthanide aluminum perovskites [J]. *Phys. Chem. Chem. Phys.*, 2019, 21(5): 2372-2377.

[13] ZHAO F Y, SONG Z, LIU Q L. Novel Cr^{3+}-activated far-red emitting phosphors with β-$Ca_3(PO_4)_2$-type structure for indoor plant cultivation [J]. *Int. J. Miner. Metall. Mater.*, 2022, 29(6): 1286-1294.

[14] ZHOU H, CAI H, ZHAO J, *et al*. Crystallographic control for Cr^{4+} activators toward efficient NIR-Ⅱ luminescence [J]. *Inorg. Chem. Front.*, 2022, 9(9): 1912-1919.

[15] AVRAM N M, BRIK M G. *Optical Properties of 3d-ions in Crystals: Spectroscopy and Crystal Field Analysis* [M]. Berlin: Springer, 2013.

[16] BRIK M G, MA C G. *Theoretical Spectroscopy of Transition Metal and Rare Earth Ions: from Free State to Crystal Field* [M]. New York: Jenny Stanford Publishing, 2020.

[17] SONG Z, WANG Z Z, HE L Z, *et al*. After-glow, luminescent thermal quenching, and energy band structure of Ce-doped yttrium aluminum-gallium garnets [J]. *J. Lumin.*, 2017, 192: 1278-1287.

[18] SONG Z, XIA Z G, LIU Q L. Insight into the relationship between crystal structure and crystal-field splitting of Ce^{3+} doped garnet compounds [J]. *J. Phys. Chem.* C, 2018, 122(6): 3567-3574.

[19] XIA Z G, MEIJERINK A. Ce^{3+}-doped garnet phosphors: composition modification, luminescence properties and applications [J]. *Chem. Soc. Rev.*, 2017, 46(1): 275-299.

[20] 薛秉国, 吕清洋, 王婷婷, 等. 钆铝石榴石(GdAG)基发光材料研究进展[J]. 发光学报, 2020, 41(12): 1538-

1553.

XUE B G, LYU Q Y, WANG T T, *et al*. Research progress of $Gd_3Al_5O_{12}$ based luminescent materials [J]. *Chin. J. Lumin.*, 2020, 41(12): 1538-1553. (in Chinese)

[21] ZHANG D, MA X X, ZHANG Q, *et al*. Influence of Zn/Al molar ratio on the structural and photoluminescence performances of $Zn_xAl_2O_4$:Cr^{3+} phosphors [J]. *J. Alloys Compd.*, 2016, 688: 581-587.

[22] SENDEN T, BROERS F T H, MEIJERINK A. Comparative study of the Mn^{4+} $^2E \rightarrow {}^4A_2$ luminescence in isostructural $RE_2Sn_2O_7$:Mn^{4+} pyrochlores (RE^{3+}=Y^{3+}, Lu^{3+} or Gd^{3+}) [J]. *Opt. Mater.*, 2016, 60: 431-437.

[23] WANG S X, SONG Z, KONG Y W, *et al*. Crystal field splitting of $4f^{n-1}5d$-levels of Ce^{3+} and Eu^{2+} in nitride compounds [J]. *J. Lumin.*, 2018, 194: 461-466.

[24] DORENBOS P. Crystal field splitting of lanthanide $4f^{n-1}5d$-levels in inorganic compounds [J]. *J. Alloys Compd.*, 2002, 341(1-2): 156-159.

宋振(1986-),男,山东乳山人,博士,副教授,2014年于北京科技大学获得博士学位,主要从事固体光谱学及发光材料构效关系的研究。

E-mail: zsong@ustb.edu.cn

刘泉林(1970-),男,山东垦利县人,博士,教授,1998年于中国科学院物理研究所获得博士学位,主要从事稀土或过渡金属掺杂的无机发光材料以及长余辉发光材料的研究。

E-mail: qlliu@ustb.edu.cn